Superconducting Radio-Frequency Cavities

Hasan S. Padamsee

Laboratory for Elementary Particle Physics, Cornell University, Ithaca, New York 14853; email: Hsp3@cornell.edu

Annu. Rev. Nucl. Part. Sci. 2014. 64:175–96

First published online as a Review in Advance on June 27, 2014

The *Annual Review of Nuclear and Particle Science* is online at nucl.annualreviews.org

This article's doi: 10.1146/annurev-nucl-102313-025612

Keywords

accelerators, niobium, gradients, quality factor, design, applications

Abstract

Superconducting cavities have been operating routinely in a variety of accelerators with a range of demanding applications. With the success of completed projects, niobium cavities have become an enabling technology, offering upgrade paths for existing facilities and pushing frontier accelerators for nuclear physics, high-energy physics, materials science, and the life sciences. With continued progress in basic understanding of radio-frequency superconductivity, the performance of cavities has steadily improved to approach theoretical capabilities.

Contents

1. INTRODUCTION

1.1. General Benefits of Superconducting Radio-Frequency Cavities to Particle Accelerators

Superconducting radio-frequency (SRF) cavities excel in applications requiring continuous-wave (cw) or long-pulse (>10-μs) accelerating fields (gradients) above a few million volts per meter. Because the ohmic power loss over the cavity walls increases as the square of the accelerating voltage, copper cavities become uneconomical when the demand for voltage increases with particle energy. The surface resistance of a superconducting cavity is many orders of magnitude lower than that of copper with intrinsic quality factors (Q_0), defined in the following section, in the range from 10^9 to 10^{10}. After accounting for the refrigerator power, a net gain factor of several hundred remains in the overall operating power for SRF cavities.

Copper cavities are limited to gradients near 1 MV m^{-1} in cw and long-pulse operation because the capital cost of the RF power and the related operating cost become prohibitive. The surface temperature becomes excessive, causing vacuum degradation, stresses, and metal fatigue due to

thermal expansion. However, copper cavities offer much higher accelerating fields ($\sim$100 MV m^{-1}) for short-pulse (microsecond) and low–duty factor (<0.1%) applications.

SRF cavities offer another important advantage: The presence of accelerating structures has a disruptive effect on the beam, limiting the quality of the beam in aspects such as energy spread, beam halo, and maximum current. SRF systems can be shorter and may therefore impose less disruption. By virtue of low wall losses, SRF cavities can be designed with large beam holes to reduce beam disruption. For a general review of SRF science and technology, see two textbooks (1, 2) and recent reviews (3–5).

1.2. Figures of Merit for Cavity Performance

Several important figures of merit characterize cavity performance. The accelerating voltage V_c is the ratio of the maximum energy gain per cell to the particle's charge. The accelerating gradient E_{acc} is the ratio of V_c to the optimal cell length, typically $\beta\lambda/2$, where β and λ are the particle velocity and RF wavelength at the resonance frequency of the cavity, respectively. Thus,

$$E_{acc} = \frac{V_c}{\beta\lambda/2}.$$

The RF power dissipation P_c is characterized by the quality factor Q_0, which provides the number of RF cycles (multiplied by 2π) required to dissipate the energy U stored in the cavity:

$$Q_0 = \frac{\omega_0 U}{P_c} = \frac{\omega_0 \mu \int_V |\mathbf{H}(\mathbf{r})|^2 \mathrm{d}V}{\oint_A R_s |\mathbf{H}(\mathbf{r})|^2 \mathrm{d}A}.$$

The RF magnetic field $\mathbf{H}(\mathbf{r})$ for the mode with angular frequency $\omega_0 = 2\pi f_0$ is integrated over the cavity volume V and surface A. The surface resistivity R_s quantifies RF power and depends only on the frequency and intrinsic material properties. It remains the only material-dependent term to cast the quality factor in terms of a geometry factor, G, as

$$Q_0 = \frac{G}{\langle R_s \rangle}.$$

Surface resistance values ranging from $\sim$1 to 10 nΩ and corresponding Q values between $\sim 10^9$ and 10^{11} can be achieved with SRF cavities. The geometry factor G is determined only by the shape of the cavity. The shunt impedance R_{sh} relates P_c to the accelerating voltage:

$$P_c = \frac{V_c^2}{R_{sh}}.$$

The geometric shunt impedance, R_{sh}/Q_0 (R/Q), can be recast as

$$R_{sh}/Q_0 = \frac{V^2}{\omega_0 U}.$$

R/Q depends only on the cavity's shape, and it should be maximized for a good cavity design. The power loss is then

$$P_c = V_c^2 \frac{R_s}{(R_{sh}/Q_0)G}.$$

Maximizing both R/Q and G during cavity design leads to low RF power dissipation.

Two very important figures of merit, E_{pk}/E_{acc} and B_{pk}/E_{acc}, are the ratios of the peak surface electric and magnetic fields, respectively, to the accelerating gradient. A high surface electric field can cause performance-degrading field emission of electrons. A high surface magnetic field may

limit the cavity's ultimate gradient performance by setting off the breakdown of superconductivity through overheating at a defect or through a magnetic transition to the normal state.

2. BASIC PHYSICS OF RADIO-FREQUENCY SUPERCONDUCTIVITY

The remarkable properties of superconductivity are due to the condensation of charge carriers into Cooper pairs, which move without friction—hence the zero-resistance hallmark of superconductivity. At $T = 0$ K, all charge carriers condense into pairs. At higher temperatures, pairs break up. The fraction of unpaired carriers increases exponentially with temperature as $e^{-\Delta/kT}$, where 2Δ is the energy gap of the superconductor, that is, the energy needed to break up the pairs. Above T_c, none of the carriers are paired, bringing about the normal conducting state. In this simplified picture, known as the London two-fluid model (6), when a dc field is turned on, the pairs carry all the current, shielding the applied field from the normal (unpaired) electrons. Electrical resistance vanishes because Cooper pairs move without friction. In the case of RF currents, however, dissipation does occur for all $T > 0$ K, although it is very small compared with the normal conducting state. Although Cooper pairs move without friction, they do have inertial mass. Forces must be applied to bring about alternating directions of current flow. Therefore, an ac electric field will be present in the skin layer to continually accelerate and decelerate the normal carriers, leading to dissipation that is proportional to the square of the RF frequency. A simplified form of the temperature dependence of R_s for $T_c/T > 2$, and for frequencies much smaller than $2\Delta/h \approx 10^{12}$ Hz (where h is the Planck constant), is (7)

$$R_s = A(1/T) f^2 e^{-\Delta(T)/kT} + R_0.$$

Here, A is a constant that depends on material parameters. The operating temperature is chosen so that the temperature-dependent part of R_s is reduced to an economically tolerable value. R_0, referred to as the residual resistance, is influenced by several factors (Section 8.1).

Fifty years ago, Bardeen, Cooper & Schrieffer (BCS) (8) put forward the first quantum-mechanical theory that successfully explained many properties of superconductivity, including RF surface resistance. At any given temperature and frequency, the magnitude of the surface resistance also depends on material parameters, such as the London penetration λ_L (~30 nm for pure niobium), intrinsic coherence length ξ_0 (64 nm for pure niobium), Fermi velocity, and in particular the electron mean free path (ℓ), which characterizes material purity. From these parameters, the BCS surface resistance can be calculated numerically (9–11). In the "dirty regime" ($\ell \ll \xi$), the surface resistance decreases with increasing ℓ. When the mean free path becomes larger than the coherence length, the surface resistance starts to show anomalous behavior, increasing with mean free path according to BCS. The clean limit applies to high-purity niobium [residual resistance ratio (RRR) > 300] commonly used for cavities. As discussed further below (Section 8.2), for the best high-field performance, cavities are generally baked at 100 to 120°C for 48 h to reduce the so-called high-field Q slope. After baking, the physics of the niobium RF surface changes from the "clean limit" to the "dirty limit" ($\ell \ll \xi_0$).

3. CAVITY DESIGN PRINCIPLES

Two classes of considerations govern SRF structure design: the accelerator application and the SRF properties (4, 5). Typical accelerator aspects are the velocity of the particle under acceleration, the desired voltage, the duty factor of operation, the beam current, and the beam power. For proton accelerators there are also beam-loss requirements and transition energies from one cavity type to another. The main design choices are cavity frequency, cavity shape, number of cells, beam

Figure 1

Nine-cell TESLA accelerating structure with an input power-coupling port at one end and a higher-order mode coupler at each end (12).

aperture, operating gradient, and operating temperature. Properties of the beam, such as bunch length, influence the wake fields and higher-order mode (HOM) impedances to play a role in the selection of the operating frequency. Typical SRF cavity properties are R_s, E_{pk}, and H_{pk} at the design accelerating field. Electromagnetic software packages for modeling cavities exist in two and three dimensions. Mechanical properties also play a role in aspects of design (Section 4.0).

In general, there are many trade-offs between competing requirements. For example, the choice of a low frequency increases the voltage gain per cell, the beam energy acceptance, and beam quality while decreasing RF losses and beam losses. However, the choice of a low frequency increases structure size (cost) and the microphonics level, making RF control more challenging. A large aperture improves the propagation of HOMs out of the structure but lowers the fundamental-mode shunt impedance and increases E_{pk} and H_{pk}.

3.1. Basic Cavity Types

There are three major classes of SRF structures: high-, medium- and low-β structures (here, $\beta = v/c$, where v is the speed of the particle and c is the speed of light). **Figures 1** and **2** show practical geometries for each type, spanning the full velocity range of particles (4, 5).

The high-β structure (**Figure 1**) is used for the acceleration of electrons, positrons, or high-energy protons with $\beta \sim 1$. It consists of a chain of coupled cells operating in the TM_{010} mode, in which the phase of the instantaneous electric field in adjacent cells is shifted by π to preserve acceleration as a charged particle traverses each cell in half an RF period. The cell length is $\beta\lambda/2$. Typical values of E_{pk}/E_{acc} range from 2.0 to 2.5, and values of H_{pk}/E_{acc} range from 4 to

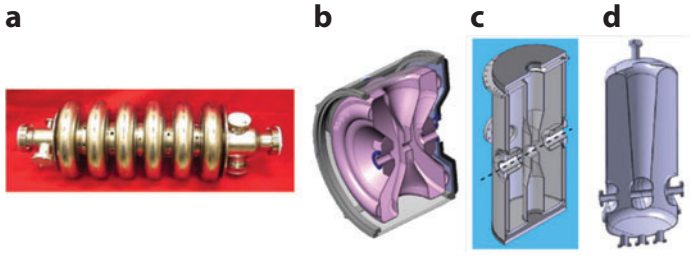

Figure 2

Medium- to low-β structures. (*a*) The 805-MHz, $\beta = 0.62$ elliptical cavity for SNS (14). (*b*) The 325-MHz, $\beta = 0.22$ single-spoke resonator for the Fermilab high-intensity proton accelerator (16). (*c*) Three-dimensional schematic of a 176-MHz, $\beta = 0.09$ half-wave resonator (17). (*d*) Three-dimensional schematic of the 88-MHz, $\beta = 0.12$ quarter-wave resonator for SPIRAL-II (18).

4.5 mT MV^{-1} m^{-1}. Special shapes have been developed to reduce H_{pk}/E_{acc} to 3.5 to 3.8 mT MV^{-1} m^{-1} by rounding the equator to expand the surface area of the high–magnetic field region (13).

Figure 1 shows the nine-cell accelerating structure (12) developed by the TESLA Collaboration and used at the Free-Electron Laser in Hamburg (FLASH) and the European X-Ray Free Electron (XFEL) project; it may also be used at the International Linear Collider (ILC). Input coupler devices on the beam tubes bring RF power into the cavity, HOM couplers extract and damp the HOMs excited by the beam, and the smaller ports carry pickup probes to sample the cavity field for regulation and monitoring. Single-cell cavities also find accelerator applications, for example, in high-current ring colliders such as CESR, KEK-B, and many storage-ring light sources. For a review of high-β design cavity aspects, see Reference 13.

3.2. Medium-β Ellipticals

Medium-β structures ($0.6 < \beta < 0.9$), such as the one at Spallation Neutron Source (SNS) at Oak Ridge National Laboratory (14), are used for protons with energies lower than 1 GeV. With a gap length of $\beta\lambda/2$, these "foreshortened" $\beta \sim 1$ structures (**Figure 2*a***) must efficiently accelerate particles whose velocity changes along the accelerator. Several geometries are needed, each of which is optimized for a particular velocity range. The lower limit of usefulness for the compression approach is $\beta \sim 0.5$, when the vertical flat walls make the structure mechanically unstable. As the cells compress (15), E_{pk}/E_{acc} increases from its typical value of 2–2.5 for $\beta = 1$ up to 3–4 for $\beta = 0.5$. For an accelerating field of 1 MV m^{-1}, B_{pk} increases from 4.0–4.5 mT for $\beta = 1$ to 6–8 mT for $\beta = 0.5$.

3.3. Medium-β Spoke Resonators

For $0.2 < \beta < 0.5$, spoke resonators with single or multiple gaps are good candidates (**Figure 2*b***). A spoke resonator consists of a cylindrical vessel, coaxial with the beam axis, loaded by ($\lambda/2$)-long spoke elements oriented perpendicular to the beam axis. Each element is a half-wavelength resonant TEM transmission line. **Figure 2*b*** shows a single-spoke 325-MHz resonator at $\beta = 0.22$ for the high-intensity proton linear accelerator (linac) that is under construction at Fermilab (16). In the multiple-spoke resonator, the loading elements are rotated by 90° from one to another. The distance between the centers of the spokes is $\beta\lambda/2$. The H_{pk} value of the spokes is typically ~6–9 mT MV^{-1} m^{-1}, and their E_{pk}/E_{acc} is ~3–6.

3.4. Low-β Structures

Low-velocity structures are used for particles moving at a small fraction (0.01 to 0.2) of the speed of light. Because the accelerating gap is $\beta\lambda/2$, low frequencies are necessary to provide a significant acceleration length at 4.2 K operation. However, 2 K operation offers substantially higher Q values.

Heavy-ion accelerators must efficiently accelerate particles whose velocity changes along the accelerator and a variety of ions with different velocity profiles. Several structure geometries are needed, each of which must be optimized for a particular velocity range. Many low-β structures, namely half-wavelength resonators (HWRs) (**Figure 2*c***) and quarter-wavelength resonators (QWRs) (**Figure 2*d***), evolve from the resonant transmission line and operate in a TEM-like mode (17, 18). For reviews of aspects of low- and medium-β design, see References 15, 19, 20, and 21.

3.4.1. Quarter-wavelength resonators. A QWR derives from a coaxial line, $\lambda/4$ in length, shortened at one end to form a resonator with a maximum electric field at $\lambda/4$, where the accelerating gaps are located. A small aperture provides high shunt impedance but low transverse acceptance for the beam. QWRs have covered a wide overall application range: $48 \leq f \leq 160$ MHz and $0.001 \leq \beta \leq 0.2$, with two and four gaps. Typical E_{pk}/E_{acc} values are ~3–5, and H_{pk}/E_{acc} values are ~6–10 mT MV^{-1} m^{-1}. Because they are asymmetric structures, QWRs have asymmetric fields that produce undesirable beam steering. Compensation can be obtained by gap shaping.

3.4.2. Half-wavelength resonators. An HWR is equivalent to two quarter waves facing each other; it provides the same accelerating voltage as a QWR but has almost twice the power dissipation. The symmetry of the structure cancels steering and permits the use of HWRs at β values ranging from 0.2 to 0.5, above the customary range for QWRs. HWRs also have better mechanical vibration properties compared with QWRs.

4. MECHANICAL ASPECTS

The design of a superconducting cavity must take into account several mechanical factors: stresses, vibrations, and Lorentz forces. Codes such as ANSYS (**http://www.ansys.com/**) and COSMOS[1] determine the mechanical properties. The cavity must be able to withstand stresses from the differential pressure between the beam-pipe vacuum and the atmosphere. Differential thermal contraction from cooldown induces stress on cavity walls. Mechanical vibrations (microphonics) of the cavity and the cavity–cryomodule system must also be taken into account. External vibrations couple to the cavity and excite mechanical resonances, which modulate the resonant frequency to induce ponderomotive instabilities (22). These instabilities translate into amplitude and phase modulations of the field and are especially significant for operation with a narrow RF bandwidth. Lorentz-force detuning becomes important in high-β cavity designs for high-field pulsed operations (23) and cw applications requiring fast phase-lock. Surface currents interact with the magnetic field to exert a Lorentz force on the cavity wall to change the cavity volume and frequency. These currents are dealt with by the proper choice of wall thickness or through the addition of stiffening rings or ribs at locations of high strain. Feed-forward and feedback in the tuning systems deal with the remaining frequency shifts. Stiffeners also raise the cavity's mechanical resonant frequencies so that they no longer couple to sources of low-frequency external vibration, such as mechanical pumps.

5. STANDARD CAVITY FABRICATION

We first describe methods that have been successfully used to fabricate large numbers of cavities, then discuss alternate methods. Niobium sheets may be ordered from several suppliers to meet well-defined cavity specifications (24). The sheets are inspected for flatness, uniform grain size (typically 50 μm), near-complete recrystallization, RRR value (>300; RRR is related to niobium purity), and good surface quality (absence of scratches). Because the many fabrication stages can embed defects, each sheet undergoes eddy-current scanning; the better side of the sheet is selected for the RF surface. Not all laboratories follow the rigorous eddy-current scanning procedure. Half-cells are stamped, spun, or hydroformed; checked with a coordinate-measuring machine for the

[1]COSMOS, Structural Research and Analysis Corp., 3000 Ocean Park Boulevard, Suite 2001, Santa Monica, California 90405-3030.

correct shape; then trimmed for weld preparations. Soaking the half-cells in dilute hot sulfuric acid for a few hours removes embedded iron particles. The half-cells are checked by a "rust test" for any remaining iron inclusions by soaking in water for 12 h. Cavity parts are given a light (20-μm) buffered chemical polishing (BCP) etch (Section 6) to prepare for electron-beam welding, then rinsed, dried in a clean room, and kept clean in sealed nylon bags. Electron-beam welding is a critical process with carefully developed parameters. To prevent RRR degradation, the vacuum in the electron-beam welder should be lower than 2×10^{-5} torr. All welds are inspected for complete, smooth underbeads; flatness on the inside; and the presence of weld spatter.

For a given amount of stored energy in the cavity, it is necessary to have equal fields in each cell so that the accelerating voltage is maximized and the peak fields are minimized. This "flat" field profile is achieved when the cells are properly tuned relative to one another. Each cell is tuned by mechanical squeezing or stretching.

Most low-β resonators are made from bulk niobium with high (150–300) RRR. Fabrication of parts includes machining, forming, rolling, and welding. Recently, a wire electric-discharge machining method has been developed in collaboration with industry (5); compared with traditional machining, this technique lessens the likelihood of foreign-material inclusion. Parts are joined together by electron-beam welding in high vacuum.

6. PREPARATION

A completed cavity goes through many steps before it is ready for RF testing. The inside surface, especially the weld quality, is inspected optically. Mechanical measurements ensure straightness and correct dimensions. The field profile is checked and adjusted. The goal is 98% field flatness.

The superconducting penetration depth for niobium is only ~40 nm. It is of the utmost importance to obtain a high-quality surface. Niobium cavities undergo an initial etching stage (100–150 μm) to remove the surface-damage layer from the sheet and half-cells (25, 26). Methods used for material removal are standard BCP, electropolishing (EP) (27), and centrifugal barrel polishing (CBP) (28). By far the best method is EP, which leads to the highest gradients. However, BCP is simpler than EP and CBP.

BCP is chemical etching with a mixture of hydrofluoric acid (HF) (40% concentration), HNO_3 (65%), and H_3PO_4 (85%) in a volumetric ratio of either 1:1:1 or 1:1:2. The process is exothermic so that good heat exchange and stirring are necessary for uniform material removal and for keeping the acid temperature below 15°C to prevent excess hydrogen uptake (Section 8.1). Because the etch rate depends on crystal-grain orientation, BCP yields sharp grain-boundary steps of 1 to 2 μm and several micrometers at the weld.

EP is carried out with an acid mix of HF (40%) and H_2SO_4 (98%), in a ratio of 1:9, as the electrolyte. The niobium cavity serves as the anode, and a high-purity aluminum cathode is inserted into the cavity. In a typical arrangement, the cavity and the cathode are in a horizontal orientation, with electrolyte filling ~60% of the cavity. The assembly is slowly rotated to enable uniform etching and polishing of the surface. The acid is circulated to an external reservoir, where it is cooled. Nitrogen gas is circulated via the cathode structure to expel the hydrogen produced. Steps at the grain boundaries are reduced to below 0.2 μm. After EP, sulfur residues (29) must be removed with ultrasonic degreasing for a couple of hours in ethanol (30) or in detergent and water (**https://indico.desy.de/conferenceDisplay.py?confId=200**). EP in a vertical orientation is somewhat simpler and is under development. Gradients of 35 MV m^{-1} have been demonstrated in nine-cell cavities (31, 32).

Tumbling or CBP removes irregularities at welds, pits, and mild scratches. The slow rate of material removal is highly dependent on the tumbling medium and rotation speeds. The final

finish can be mirrorlike, with 10-nm roughness, but this quality does not yield better performance than EP. Additional chemical etching by BCP or EP (20–50 μm) is still necessary to remove the tumbling abrasive embedded in the surface (33). CBP has successfully been used to repair cavities with mechanical defects, such as pits, and to bring them to high-field (>30 MV m^{-1}) performance (33, 34).

After chemical etching and rinsing, high-pressure water rinsing (HPR) is carried out for several hours with particulate-free (0.1-μm-or-better filters) deionized water at a nozzle pressure of ~100 bar to remove chemical residues (35, 36). HPR is performed in a Class 100 (or better) clean room to prevent dust contamination (a Class 95 clean room must contain no more than 100 particles with size greater than 0.5 μm). All preparation procedures for bulk material removal carry a risk of hydrogen absorption, so furnace treatment is necessary to remove the hydrogen and prevent *Q* disease (see Section 8). The cell-to-cell field profile is remeasured and readjusted. The final chemical treatment is a light etch (~20–30-μm material removal) by either BCP or EP, depending on the target field level.

After the final chemical treatment and thorough rinsing with high-purity (>18 MΩ-cm resistivity) water, the cavity is transported (after the outside is cleaned) to a Class 10–100 clean room, where the inside surface again undergoes HPR (100 bar) with high-purity water jets for many hours. The main goal is to scrub the chemical residues and particulate contaminants, which may cause field emission or thermal breakdown (Section 9). After HPR, the cavity dries in the clean room before being assembled with components for testing.

To reach the highest fields, an electropolished cavity needs to be baked at 120°C for 48 h (37, 38). Temperatures up to 140°C have been used with shorter baking time (several hours). This mild baking step provides several benefits: It reduces the processing time for multipacting (MP) by degassing water from the surface; it reduces the BCS surface resistance for higher *Q* values; and most importantly, it removes the high-field *Q* drop (see Section 8.2). Baking is normally carried out with the inside of the cavity in a good vacuum (~10^{-8} torr) or in 1 atm of high-purity argon gas. In some cases, a second round of HPR takes place after assembly of the necessary flanges and the field monitor probe. The cavity is then ready for evacuation for RF tests. One must take great care to avoid recontamination during the subsequent cavity handling, component assembly, and installation (39).

With moderate field requirements (B_{pk} < 100 mT), many low-β cavities are prepared by BCP. In some cases, niobium subcomponents are electropolished individually and then welded together. A final 5–10-min standard BCP is used to remove the welding residues (5).

7. ALTERNATE FABRICATION METHODS

Several alternate cavity-fabrication methods that have been developed to reduce cost include thin-film deposition by magnetron sputtering of niobium films on copper, hydroforming, and spinning from niobium tubes. The last two methods limit expensive machining and electron-beam welding, moving toward seamless cavities. The availability of large-grain niobium has the potential to simplify the sheet production sequence and, consequently, to reduce the cost of materials and susceptibility to defects from the various steps of sheet manufacturing.

7.1. Thin Films on Copper

Thin films of niobium on copper (40) offer several advantages over bulk niobium: higher thermal stability from the high–thermal conductivity copper substrate and reduced cost of materials, which can be substantial for low-frequency (<700-MHz) cavities. The niobium layer's resistance to

external dc magnetic fields also decreases by an order of magnitude due to its high H_{c2}, reducing the magnetic shielding requirements for cryomodules. The base copper cavity is made by the same methods as niobium cavities. One must exercise caution to begin with a smooth (EP) copper surface without pores and inclusions. The best cavities made to date were produced by cylindrical magnetron sputtering. More than 300 350-MHz cavities for LEP-II have been created. These cavities reached 7.5 MV m^{-1} at Q values of 2×10^9. Niobium-on-copper cavities have also been developed for low-β structures at ALPI and are under development for HI-ISOLDE at CERN (41).

Niobium-on-copper cavities have shown strong Q degradation with field. The best results have been obtained at 1,500 MHz; the Q value falls from 10^{10} at 15 MV m^{-1} to 3×10^9 at 20 MV m^{-1}. The reason for the persistent slope has not yet been identified, although many explanations have been suggested. RF losses may arise from "weak links" between the very fine (10–100-nm) grains. More recently, niobium films grown by energetic deposition (42, 43) have shown an epitaxial character with low defect density, as measured by high (200–400) RRR, compared with magnetron films with lower (~20) RRR. Cavities have yet to be made with this technique.

7.2. Hydroforming and Spinning

Hydroforming of a weld-free cavity starts with a tube of diameter intermediate between iris and equator (44–46). This process occurs in two stages: reduction of the tube diameter (necking) to form the iris area and hydraulic expansion (hydroforming) for the equator area. Several single-cell 1.3-GHz cavities have been manufactured without intermediate annealing. Single-cell cavities made by hydroforming (47) or spinning, followed by standard preparation treatments for niobium, had E_{acc} values of ~40 MV m^{-1} (44)—comparable to the best results attained by cavities made with standard methods. DESY extended hydroforming to three-cell, 1.3-GHz cavities and built three nine-cell prototypes by welding three-cell units. These cavities achieved E_{acc} values of ~30–35 MV m^{-1}. Hydroforming has also been used to fabricate cavities from niobium-on-copper-clad material (47). They use substantially less niobium, have fewer welds, and have improved thermal conductivity and stiffness from the backing copper. Attachment of end flanges or end groups containing coupler ports requires welding to the thin niobium layer. The copper backing must be completely removed and cleaned at the weld joints before electron-beam welding, which presents some difficulties. Niobium tubes with a thickness as low as 0.7 mm have been successfully welded to 2-mm-thick niobium tubing. Single-cell cavities have been built at DESY and KEK, reaching E_{acc} values of up to 40 MV m^{-1}. Temperature gradients across the cavity have to be minimized near T_c to avoid trapping the magnetic field attributed to thermoelectric currents (see Section 8).

Several single-cell and multicell weld-free cavities starting from disks and from seamless tubes (48) have been spun. After spinning, cavities must be tumbled or mechanically ground to at least 100 μm to remove surface fissures before chemical treatment. Q values higher than 10^{10} and accelerating fields higher than 40 MV m^{-1} have been reproduced with spun single-cell cavities. Starting niobium tubes of the appropriate diameter and uniform fine-grain structure are made by deep drawing, flow forming, extrusion, or a combination of these techniques.

7.3. Large-Grain Niobium for Cavities

The mechanical properties of large-grain niobium disks sliced directly from ingot by wire electrodischarge machining are adequate for forming cavity half-cells (49–52). These multiwire slicing techniques enable mass production of disks. Direct slicing from ingot reduces the probability of defect inclusions through the steps of standard sheet production: forging, grinding, rolling, and

annealing. These disks have large grains that are several centimeters in diameter. Proper tooling (51) is required to deal with ragged edges at the equator region. Sharp steps at grain boundaries, arising from nonuniform properties of different grains, must be eliminated by local grinding or CBP. Nine-cell cavities built from large-grain niobium and prepared by EP and baking have achieved performance levels comparable to that of cavities built from standard, fine-grain niobium. Several nine-cell cavities have reached accelerating gradients higher than 40 MV m^{-1}; one achieved a record 45 MV m^{-1} (52). The Q value of these cavities is also 20–30% higher (53), most likely due to the reduced flux-trapping efficiency (54). Several single-crystal 1.3-GHz cavities (50) have also been made, but their performance is not significantly better than that of standard cavities. Grain boundaries do not present a barrier for ultimate gradients, as demonstrated by the highest fields of 205 mT obtained with fine-grain single cells (55).

8. HIGH-Q PERFORMANCE

8.1. Residual Resistance

Residual resistance has several known causes: insufficient shielding of the ambient dc magnetic field, hydrogen-related Q disease, condensed gases, and a modified oxide layer. Other possible sources of residual resistance may include direct phonon generation, subgap states, or interface losses, but these need more substantiation by experiments.

When a niobium cavity is cooled in the ambient dc magnetic field, magnetic flux is trapped in the niobium at defects such as grain boundaries, vacancies, or the oxide. Experimental studies with niobium disks show that more than 80% of the flux within the volume of the metal is trapped (56). Niobium annealed at 800°C and large-grain (>1-cm) niobium trap less flux (54). The RF loss comes from the normal conducting cores of trapped dc flux lines and is ~0.3 nΩ for 1 mG at 1 GHz. These losses increase as the square root of the RF frequency, as expected from losses due to a normal conductor. Such losses can be reduced by shielding the cavity from the Earth's field, preferably to below 5 mG. Recent studies have shown that a smaller fraction of the ambient flux is trapped with faster cooling rates below T_c (57). Another mechanism for trapping flux is through thermal currents from large temperature gradients during cavity cooldown, especially when the cavity is encased in a helium vessel made of titanium, giving rise to significant thermal electromotive forces from the bimetallic combination. Thermocurrent-induced flux can also be trapped when a cavity quenches (Section 9) and regions of it warm up to well above T_c. The best way to reduce thermocurrent-induced losses is to cool the cavity down slowly through T_c. If the Q value drops after a cavity quench, the best method to restore it is to warm the cavity above T_c and then cool it down slowly (58).

An important residual loss arises when hydrogen dissolved in the bulk niobium precipitates as a lossy niobium hydride at the RF surface (59). This loss (commonly referred to as Q disease) is a subtle effect that depends on the quantity of dissolved hydrogen, the rate of cooldown through 100 K, and the amount of other interstitial impurities or atomic size defects present in the niobium. Hydrogen is absorbed effectively when the protective oxide layer is not present. Large amounts of hydrogen dissolve in niobium if the acid for BCP gets hot ($T > 15$°C) or if too much hydrogen arrives at the cavity surface during EP. CBP generates the most hydrogen.

For severe Q disease, Q values fall to 10^7 above a few megavolts per meter. Niobium hydride phases that are harmful to superconductivity form between 100 and 150 K, when the hydrogen concentration is greater than 100–200 ppm, as shown by the niobium hydride phase diagram in Reference 60. Hydride formation has recently been studied through the use of confocal optical microscopy (61, 62). Below 77 K, hydrogen mobility is low enough to arrest the growth of hydrides.

The sharp drop in the Q-versus-E curve for a cavity with strong Q disease indicates that niobium hydride regions are initially superconducting at low fields (<5 MV m^{-1}) and become normal conducting at higher fields. Low-RRR (27) niobium does not demonstrate Q disease because interstitial impurities (such as oxygen) trap hydrogen, preventing its mobility and hydride growth. Similarly, vacancies and grain boundaries are also effective hydrogen traps (63, 64). The best cure for Q disease is to bake the cavity either at 800°C for a couple of hours or at 600°C for 10 h if the small decrease in yield strength from 800°C baking cannot be tolerated.

Condensed gas is another cause of residual loss (65). It can be avoided by maintaining a good vacuum ($\sim 10^{-8}$ torr at room temperature). Baking at 120°C (Section 8.2) also increases residual resistance by a few nano-ohms because it partially converts some loss-free pentoxide into niobium suboxides (66, 67). The damaged oxide layer can be removed by rinsing the surface with HF (commercial strength, ~50%) and regrowing a fresh, low-loss pentoxide layer (68).

HF rinsing after baking at 120°C causes significant gains in final Q values. Q values of 3×10^{10} at 1.8 K were reached with several single cells (68, 69) and seven-cell 1.3-GHz cavities through application of BCP, baking at 120°C, and an HF rinsing step. Even higher Q values were obtained by a slow cooldown (<1° h^{-1} through T_c) to avoid flux trapping from thermocurrents. The Q value at 2 K was 3.5×10^{10}, which increased to 6×10^{10} at 1.8 K and 10^{11} at 1.6 K.

8.2. Q Versus E_{acc}: Low-, Medium-, and High-Field Effects

The excitation curve (Q versus E_{acc}) of a cavity in the gigahertz range generally has three distinct regions. An increase in Q (as much as 50%) is often observed at E_{acc} values below 5 MV m^{-1} and is referred to as the low-field Q slope (LFQS). It is usually followed by a gradual Q value degradation, known as the medium-field Q slope (MFQS), out to 20–30 MV m^{-1}. The Q value can drop by a factor of two between 5 and 25 MV m^{-1}. Above an onset field of ~80 mT (E_{acc} = 20–25 MV m^{-1}), the quality factor starts to decrease rapidly, even in the absence of field emission (see Section 9.1). This behavior is known as the high-field Q slope (HFQS). At the highest fields, the performance of the cavity is limited by a quench, or breakdown, of superconductivity (see Section 9.2).

The underlying cause of the LFQS is still unknown. An interesting series of experiments suggests that it originates from the metal oxide layer or interface (70). The simplest explanation for the MFQS is based on thermal feedback (71–73). The surface temperature increases due to RF heating. The exponential temperature dependence of the BCS resistance drives a thermal feedback; thermal conductivity and heat transfer at the niobium–helium interface play important roles. Thermal feedback provides a fair account of cavities in which BCS resistance dominates, that is, for $f > 2.5$ GHz or $T \sim 4.2$ K, but yields a rather weak slope compared with observations for $f \sim 1$ GHz. An intrinsic nonlinearity of R_{BCS}, due to the increase in thermally activated quasiparticles by the RF field, has been calculated in the clean limit (74), but it generally predicts a stronger-than-measured MFQS (75, 76). For high values of f, the f^2 dependence of the BCS surface resistance eventually causes thermal instability well below the RF critical field, resulting in global thermal instability (77) in which the entire high–magnetic field region of the surface approaches T_c.

Recently, there has been remarkable progress toward higher Q values at medium fields. Occasionally, 1,000°C treatments for long periods have yielded very high Q values (78). Q enhancements of single-cell and nine-cell 1.3-GHz cavities have been demonstrated via nitrogen and argon doping (at 10^{-2} torr for 10 min) at 800°C, followed by light EP of ~10 μm (79). At low fields, Q values of 4×10^{10} at 2 K and 8×10^{10} at 1.8 K were obtained in many tests. The parameters of time, temperature, nitrogen pressure, and postchemistry are still under exploration to obtain

the highest Q values. Surprisingly, this treatment also *reverses* the generally observed MFQS and has been named the anti-Q-slope effect. The underlying cause has yet to be fully understood. Enhanced Q values will greatly benefit cw applications at medium fields (see Section 10).

On the theoretical front, a reversal of the MFQS has been predicted. The BCS surface resistance has been recalculated to show that Q should increase from 0 to 100 mT due to a decrease in thermally activated quasi-particles as both the Cooper pairing energy and the density of states change with increasing velocity of the Cooper pairs (80). The LFQS and the so-called anti-Q-slope effect of the nitrogen-treated cavities may represent experimental confirmations of the new calculations. For the LFQS, the enhancement of the slope with baking at 120°C still needs to be explained. For the anti-Q-slope effect, the role of nitrogen doping needs to be elucidated.

The HFQS is present in cavities prepared by a wide variety of methods: BCP; EP; use of small-grain, single-crystal, or large-grain niobium; and even heating to 800°C. The HFQS is accompanied by strong heating in the high–magnetic field regions determined from temperature maps. There is large spatial inhomogeneity in the heating pattern. The signature property of the HFQS is its improvement with mild baking at 100–120°C for 48 h. The benefit for EP cavities is the greatest. Experimental data and models related to the high-field Q slope have been extensively reviewed elsewhere (81–84).

The most recent model explains the HFQS as a milder version of hydrogen-related Q disease. The model invokes the thin, hydrogen-rich layer (~1–20 at%) near the surface (85–87). The hydrogen segregates in the first few tens of nanometers because of the local strain induced by the oxide layer. Between 100 and 150 K, niobium hydride precipitates form in the hydrogen-rich layer at favorable nucleation sites, such as local stress centers. The T_c of niobium hydride is near 1.5 K, but the proximity effect between niobium hydride and the surrounding niobium renders the hydrides superconducting at helium temperatures (88). The onset field of the HFQS depends on the size of the hydrides, estimated to be $\geq$10 nm. Proximity superconductivity can be sustained only up to a magnetic field value that is inversely proportional to the smallest-dimension hydride ($B_c \sim 1/d$). At $B \sim 100$ mT, hydrides (starting from the largest) begin to transition to the normal conducting state. This is the onset of the HFQS. As the field rises, the smaller hydrides become normal. The 120°C baking effect is explained by the injection and diffusion of vacancies from the surface (89), which trap hydrogen, preventing it from diffusing freely to form hydrides. Additionally, the low electron mean free path from 120°C baking is attributed to the unprecipitated hydrogen, which now acts as an interstitial impurity. Before baking, all the hydrogen in the RF layer precipitates into hydrides on cooldown, resulting in a large electron mean free path value over most of the surface.

9. GRADIENT LIMITATIONS

9.1. Performance Breakthroughs

Over the past 30 years, the gradients for high-β accelerator structures have increased steadily from 3–5 MV m^{-1} in the early 1980s to 30–45 MV m^{-1} by 2012. These advances have come from several breakthroughs in our understanding of the physics of limitations, followed by innovative solutions. We provide a brief overview of these advances, then discuss more recent breakthroughs.

Before 1980, the dominant phenomenon limiting gradients was one-surface MP, in which an electron avalanche builds up within a small region of the cavity surface due to resonant electron trajectories combined with a high secondary electron–emission coefficient. The invention of the round-wall (spherical) cavity shape (90) solved this problem. In such cavities, the trajectories of electrons with this modified shape are pushed into the low–electric field region, where they cannot

gain enough energy to multiply. Even after overcoming MP, cavity gradients rose to only ~6 MV m^{-1} due to thermal breakdown (or quench) of superconductivity around defects (Section 9.2) in which RF losses dominate. The solution was to use higher–thermal conductivity, higher-purity niobium, as characterized by RRR. With the higher thermal conductivity, a given defect can tolerate a higher RF dissipation at higher gradients before driving the neighboring superconductor into the normal state (1, p. 205; 91). With higher-RRR niobium, gradients rose to ~10 MV m^{-1} when field emission (FE) took over. The Q value of a niobium cavity falls exponentially with increasing electron currents emerging from particular emitting spots on the surface. Research has shown that microparticle contaminants are the dominant sources of FE (92, 93). High pulsed power RF (~1 MW, 200 μs) was used to burn out these emitters and reach 25 MV m^{-1} in five-cell 1.3-GHz cavities (94). Micrometer-sized craters formed around the culprit FE sites yielded Q values of 10^{10}. Later, the use of HPR led to a drastic reduction in the number of FE sites and corresponding improvements in cavity gradients to ~25 MV m^{-1} (36). Above 25 MV m^{-1}, the HFQS took over, sharply decreasing the cavity Q value with field. The empirical cure to the HFQS was discovered quickly. Two steps are essential: the preparation of smooth surfaces by EP and baking of the cavity at 120°C for ~2 days. The gradients rose to 35 MV m^{-1}, with record values of 40 to 45 MV m^{-1}. Of course, the above solutions must be applied together to avoid MP, thermal breakdown, FE, and the HFQS. High pulsed power is often used during operation to process the remaining emitters and reduce X-rays (95).

High-purity, high–thermal conductivity niobium, together with HPR and clean room preparation, led to parallel progress in gradients in low-β and medium-β cavities. The gradients rose from 2–3 MV m^{-1} to 7–10 MV m^{-1}. At SNS, the gradients of $\beta = 0.62$ cavities exceeded 15 MV m^{-1}.

9.2. Quench Location and Associated Defects

Quench-causing defects are traditionally located by thermometry systems that envelop the outer wall of the cavity with many hundreds of carbon thermometers (58). After the defects are located, the cavity is dissected and the defects studied by electron microscopy. Another method for quench-location detection using oscillating superleak transducers (OSTs) was later developed (96). OSTs detect the second sound waves driven by the quench through He-II. By measuring the arrival time of each wave at three or more detectors, OSTs can determine the quench location with ~1-cm spatial resolution.

The thermometry/dissection method can reveal a panorama of defects (58). The starting material may have embedded foreign-material defects or manufacturing flaws (97). Chemical stains may be left behind from insufficient rinsing (98). Electron-beam welds may contain embedded contamination at the seam before welding (12). If done poorly, welds can produce spatter in the form of niobium balls, some of which cannot be removed by standard chemistry. Welds occasionally have voids with sharp edges that locally enhance the magnetic field; voids are occasionally found outside the weld (58). Material (e.g., metallic flakes from the power coupler) can drop into the high–magnetic field region from cavity assembly. Such material heats up in the RF field and welds to the niobium to form a quench-producing defect. Thermometry also shows defects that remain superconducting below a certain field, then suddenly heat up and lead to quench (99). The nature of these "superconducting defects" needs to be further investigated.

To avoid cavity dissection, imaging systems have been developed to take pictures of the defect inside the cavity with resolution of a few micrometers (100). Several nine-cell cavities (some from new cavity vendors) show pitlike defects that quench below 20 MV m^{-1}. The heat-affected zone near the weld has a tendency to form large voids that often originate in high-stress regions (101),

then increase to 100–200 μm during EP and retain their sharp edges (102). Such defects can be removed by CBP or by a local grinding tool (103).

9.3. Quench Field, RRR, and Surface Preparation

The correlation between higher RRR and increased quench field is clear from data taken from single-cell (104) and, later, nine-cell cavities made of fine-grain niobium and treated by BCP (12). In a pleasant surprise, the introduction of EP and 120°C baking (to cure the HFQS) also raises quench fields for cavities with lower (<200) RRR values, as discovered first with single-cell cavities (105) and subsequently with nine-cell cavities (2, p. 199), in part because of the absence of steps at grain boundaries. When a defect is located near (typically, a few micrometers from) a grain-boundary step, the local magnetic field is enhanced near the sharp step, and the quench field is lower for a given RRR. For BCP-prepared surfaces, grain boundary steps are present every 50–100 μm. With EP, the grain boundary steps are smaller (<0.2 μm) and rounded, reducing field enhancement. Another reason for the lower quench fields with BCP-prepared surfaces is the higher background heating due to the HFQS. Large-grain cavities also show an improvement in quench field at RRR values of 150 to 200 (51). Here the intergrain surface area is extremely smooth (<20 nm). For applications demanding gradients below 30 MV m^{-1}, the RRR specification may be relaxed to >150, with potential cost reduction. However, the yield for high gradients with lower RRR values has yet to be established. Another niobium specification that may be relaxed to reduce cost is the tantalum content, which can be increased from 500 ppm to 1,500 ppm. The effect of the substantial tantalum impurity on the RRR is rather benign compared with that of the interstitial elements oxygen, nitrogen, carbon, and hydrogen. One thousand ppm of tantalum is equivalent to 5 ppm of oxygen (106).

9.4. Radio-Frequency Critical Field

The prevailing definition for the RF critical field is the superheating field H_{sh}. In RF fields, a superconductor can stay in the Meissner phase with delayed flux entry because the RF period is very short (nanoseconds). The maximum field below which this metastability can persist is H_{sh}. Typically, $H_{sh} \sim H_c > H_{c1}$ for type II superconductors. H_{sh} depends on material properties via the Ginzburg–Landau (GL) parameter κ_{GL}, which is the ratio of the penetration depth (λ) to the coherence length (ξ). Both quantities depend on mean free path and temperature. According to the GL theory, H_{sh} is given by (107)

$$H_{sh} \approx 1.2 H_c, \quad \kappa_{GL} \approx 1,$$

$$H_{sh} \approx 0.75 H_c, \quad \kappa_{GL} \gg 1.$$

Above H_{c1}, vortices have to overcome the surface barrier, which ideally disappears only at H_{sh}. Thus, the lower critical field, H_{c1}, is not a limit for high-performing niobium cavities, which maintain their high Q values well above H_{c1}. However, the surface barrier to flux entry can be reduced by local defects, so local losses may arise due to vortex entry, which may explain quench sites that show no heating up to an onset field. The GL theory is valid only near T_c, but cavities operate at $T/T_c \ll 1$. The calculation for H_{sh} has been performed with the full BCS theory at low temperature (108, 109), in the clean limit, and as a function of impurities in the limit of high κ_{GL}. The result is close to the simple GL calculation, yielding $H_{sh} \sim 0.84\, H_c$ for high κ.

The fundamental RF critical magnetic field has been measured with 1.3-GHz single-cell cavities using high pulsed power to quickly (within <100 μs) raise the cavity fields well above the cw limits

(110–112). High fields can be reached before local defects create normal conducting regions. The Q value of the cavity is measured during the pulse to ensure that a significant fraction of the cavity surface is superconducting. The RF critical magnetic field is close to H_{sh}, as predicted.

In cw operation, Q values remain near 10^{10} up to surface magnetic fields of 200 mT, which is above H_c (190 mT) at 2 K and close to H_{sh}. The high Q value proves that RF flux does not enter the RF layer at H_{c1} (160 mT at 2K). Many single-cell and nine-cell 1.3-GHz cavities reach $H_{pk} = 170$ mT at high Q values. The best single-cell cavities reach 205 mT (55). All these cavities are prepared by baking at 120°C so that the electron mean free path drops to ~20 nm and κ_{GL} increases to ~3; therefore, H_{c1} is less than 100 mT after baking, confirming that H_{c1} is irrelevant as the performance limit for niobium cavities.

The results for niobium are encouraging for high-κ_{GL}, high-T_c materials such as Nb_3Sn ($T_c = 18$ K) with $\kappa_{GL} \sim 20$, $H_c = 530$ mT, and $H_{sh} = 0.84$. The value of H_{sh} is 450 mT, leading to a prediction of $H_{sh} \sim 125$ MV m^{-1} for an advanced geometry structure with $H_{pk}/E_{acc} = 3.6$ mT MV^{-1} m^{-1}. Such fields have yet to be realized, although the level of effort in this area has been very minimal. Using high pulsed power, fields of 100 mT have been reached (110, 111). However, with these fields' short coherence length, it may prove difficult for high-T_c materials to bridge good superconducting properties across imperfect regions (e.g., grain boundaries). A theoretical possibility of supporting higher–surface RF magnetic fields through the use of thin multilayer superconductor/insulator structures has been proposed (113), but more recent research (114) has shown that such superconductor/insulator layers would have $H_{c1} = 0$ and a lower H_{sh} than would be achieved using the high-T_c material as a bulk superconductor instead of an overlayer (114).

10. APPLICATIONS: PAST, PRESENT, AND FUTURE

The history of SRF application to accelerators has been described elsewhere (1–5). Over the past three decades, SRF has become the technology of choice for numerous accelerators for high-energy physics and nuclear physics, light sources, neutron sources, and high-intensity proton accelerators. Our brief review of some of these applications focuses on performance improvements.

By the year 2000, more than 700 m of superconducting cavities had been installed worldwide and had successfully operated at accelerating fields up to 7.5 MV m^{-1} for a total of more than 2.5 GV for various high-β accelerators. The two largest installations were those for LEP-2 at CERN (115) and for CEBAF at Jefferson Lab (116). The former had 288 niobium-on-copper 325-MHz cavities, and the second had 350 niobium 1,500-MHz cavities. The LEP-2 system was decommissioned when LEP was replaced by the LHC, which has 16 niobium-on-copper cavities at 400 MHz that can operate at up to 8 MV m^{-1} (117).

CEBAF is undergoing an upgrade to boost its energy to 12 GeV (118). Ten new cryomodules have been installed, each of which consists of eight seven-cell cavities of low-loss shape (3, 13) and operates in cw mode at 19.2 MV m^{-1}. Individual acceptance tests have yielded an average of 25 MV m^{-1} (3). The best seven-cell cavity with fine-grain niobium reached 43.5 MV m^{-1}. The surface preparation employed BCP but with a final step of light EP. Jefferson Lab also ran a free-electron laser (FEL) (119) with 14 kW of cw laser power in the IR band with energy recovery by recirculating nearly 1 MW of beam power—an important milestone toward energy recovery linacs (ERLs) for future light sources and electron-beam cooling applications. The best cryomodule operated cavities at 20 MV m^{-1} (3).

The TESLA (TeV Energy Superconducting Linear Accelerator) Collaboration, based at DESY (120), began developing high-gradient TESLA technology for a future high-energy superconducting linear collider. This international collaborative effort started around 1989 (121). The TESLA

Test Facility (TTF) was installed to demonstrate high-gradient operation and to generate UV light with self-amplified stimulated emission (122). In the first phase, TTF operated at 270 MeV with two modules of eight nine-cell cavities at 15 MV m^{-1}. The cavities were prepared by BCP, with the gradient limited by the HFQS. In the second phase, TTF (renamed FLASH) was upgraded to 1.2 GeV with seven modules of 56 cavities (123). Most cavities were prepared by EP and 120°C baking to operate at 23 MV m^{-1}. The best cryomodules ran at 30 MV m^{-1} (124). Fermilab contributed to FLASH a third-harmonic cryomodule with four 3.9-GHz cavities for phase-space linearization. The cavities prepared by BCP were emission free to 20 MV m^{-1} and quench free to >24 MV m^{-1} (125) for operation at 14 MV m^{-1}.

The success of FLASH became the basis of the most ambitious SRF project to date, XFEL, which will be a 17.6-GeV linac with 800 TESLA-type cavities running at 23.6 MV m^{-1} (126). Construction has begun, and the first 100 cavities have been qualified. The average maximum gradient is 32 ± 5.5 MV m^{-1}.

XFEL will be a strong proof-of-principle accelerator for a future 500-GeV ILC (127). The technical design report for the ILC was completed in June 2013. The ILC is based on 17,000 cavities at 31.5 MV m^{-1}. The yield for large-scale production has improved steadily during the past decade, nearing 90%. There are plans to upgrade the ILC to 1 TeV with higher-gradient (45–50 MV m^{-1}) cavities. The gradient has been demonstrated with single cells of low-loss and reentrant shapes (13).

Whereas FLASH is a pulsed FEL, a cw FEL at 4 GeV would be an attractive future X-ray source, and one such FEL (the LCLS-II light source) has been planned at SLAC. A moderate gradient of 16 MV m^{-1} would keep the dynamic heat load manageable. For a Q value of 3×10^{10}, the 1.8 K heat load would be nearly 3 kW. Efforts are under way to reliably reach the same high Q value at 2 K; these include the new methods of doping niobium with nitrogen or argon (79).

High-luminosity electron–positron colliders and high-current storage-ring light sources have been operating at 5 to 8 MV m^{-1} at Cornell University, KEK in Japan, and IHEP in China, as well as at Taiwan Light Source, the Canadian Light Source, DIAMOND in the United Kingdom, Shanghai Light Source in China, Pohang Light Source in Korea, and SOLEIL in France (128). NSLS-II at Brookhaven National Laboratory is preparing to install similar systems. Another path for future light sources is via ERLs, which are efficient because of their high brightness and/or ultrashort–pulse length light sources (129, 130). Cornell is developing a 100-mA hard X-ray light source driven by an ERL. This 5-GeV ERL will have 384 seven-cell SRF cavities running in cw mode at 16.2 MV m^{-1}. A prototype injector with five two-cell cavities at 1,300 MHz has operated in cw mode at 15 MV m^{-1} both without a beam and with a world-record beam current of 75 mA at 4 MV m^{-1}. Several ERL prototype projects have been begun at KEK, Brookhaven National Laboratory, Berlin, and Beijing. High-intensity beams for ERLs have spurred explorations for electron cooling applications and for electron–ion colliders, such as an upgraded RHIC.

SNS, a high-flux spallation neutron source that uses medium-β cavities, has been running for 7 years as the world's first SRF linac for pulsed proton beams (131, 132). SNS has a total of 81 six-cell cavities operating at 805 MHz: 33 medium-β (0.61) and 48 high-β (0.81) cavities. The linac performs reliably at ~15 MV m^{-1} but is limited by field-emission heating effects. In Europe, the planned European Spallation Source (ESS) at Lund (133) will have 2.5 GeV of SRF cavities and an ultimate beam power of up to 5 MW.

A high-intensity proton linac for neutrino beam lines is under construction at Fermilab. A recent test of single-spoke 325-MHz resonators at $\beta = 0.22$ exceeded the project requirements of $E_{acc} = 12$ MV m^{-1} and $Q = 5 \times 10^9$ with test fields of $E_{acc} = 22$ MV m^{-1} and $B_{pk} = 125$ mT (134). High-intensity SRF proton linacs are suitable for a variety of future needs: transmutation applications for treatment of radioactive nuclear waste, nuclear energy production using thorium

fuel, high-intensity muon sources for muon storage ring–based neutrino factories, and eventually a multi-TeV energy scale muon collider.

Since the 1970s, low-β superconducting linacs providing precision heavy-ion beams have been some of the most successful applications. ATLAS at Argonne National Laboratory has been operating for more than 30 years (5). Others include ALPI at INFN in Italy, ISAC and ISAC-II at TRIUMF in Canada, and IUAC in India. More than 250 superconducting low-β resonators are operating around the world. ATLAS's energy was upgraded with a single 5-m-long cryomodule containing seven 109-MHz $\beta = 0.15$ QWR resonators at 7.6 MV m^{-1} (135). Improvements continue with 72-MHz $\beta = 0.077$ quarter-wave cavities (136). The maximum cw accelerating gradients are 13.7 MV m^{-1} at 4 K and 15.5 MV m^{-1} at 2 K (limited by available X-ray shielding).

Radioisotope beam (RIB) facilities using low-β cavities are being installed for the SPIRAL2 (137) project at GANIL, France, and are under development for the ReAccelerator and FRIB (138) at Michigan State University in the United States. SPIRAL2 will have 12 $\beta = 0.07$ and 14 $\beta = 0.12$ 88-MHz QWRs operating at 4.2 K at 6.5 MV m^{-1}. During vertical tests, the cavities achieved gradients above 10 MV m^{-1} with $Q \sim 1 \times 10^9$ at 4.2 K—well above design. FRIB is the most ambitious RIB facility under construction; it may become the world's largest heavy-ion accelerator. It will have 100 QWRs ($\beta = 0.041$ and 0.085) and 216 HWRs in 45 cryomodules. More than 20 prototypes have been tested to gradients above 7 MV m^{-1}—well above operating requirements.

11. CONCLUSIONS

SRF has entered a golden age, with major progress in structure design and operation across the wide spectrum of cavity types from low β to high β. Fundamental progress in SRF science has led to performance improvements in both gradients and Q values for all cavity types. The total installed voltage projects are on their way to increasing from 7 GeV to more than 30 GeV after completion of XFEL, ESS, and LCLS-II.

DISCLOSURE STATEMENT

The author is not aware of any affiliations, memberships, funding, or financial holdings that might be perceived as affecting the objectivity of this review.

ACKNOWLEDGMENTS

My work is supported by the National Science Foundation (NSF) under NSF Sponsor Agreement ID PHY-0969959 and by the US Department of Energy (DOE) under DOE Sponsor Agreement ID DE-SD0008431.

LITERATURE CITED

1. Padamsee H, Knobloch J, Hays T. *RF Superconductivity for Accelerators*. New York: Wiley. 2nd ed. (2008)
2. Padamsee H. *RF Superconductivity: Science, Technology and Applications*. New York: Wiley (2009)
3. Reece CE, Ciovati G. *Rev. Accel. Sci. Technol.* 5:285 (2012)
4. Belomestnykh S. *Rev. Accel. Sci. Technol.* 5:147 (2012)
5. Kelly M. *Rev. Accel. Sci. Technol.* 5:185 (2012)
6. London F, London H. *Proc. R. Soc. Lond. A* 149:71 (1935)
7. Mattis DC, Bardeen J. *Phys. Rev.* 111:412 (1958)
8. Bardeen J, Cooper LN, Schrieffer JR. *Phys. Rev.* 108:1175 (1957)

9. Halbritter J. *Z. Phys.* 266:209 (1974)
10. Halbritter J. *Z. Phys.* 238:466 (1970)
11. Kneisel P. *Proc. Workshop Push. Limits RF Supercond.*, p. 206. Argonne, IL: Argonne Natl. Lab. (2004)
12. Aune B, et al. *Phys. Rev. Spec. Top. Accel. Beams* 3:092001 (2000)
13. Belomestnykh S, Shemelin V. *Proc. 12th Workshop RF Supercond.* (*SRF2005*), p. 2. Ithaca, NY: Cornell Univ. Press (2005)
14. Ciovati G, et al. *Proc. 2001 Part. Accel. Conf.* (*PAC2001*), p. 484. Piscataway, NJ: IEEE (2001)
15. Delayen JR. *Proc. 10th Workshop RF Supercond.* (*SRF2001*), p. 152. Tsukuba, Jpn.: KEK (2001)
16. Apollinari G. *Proc. 12th Workshop RF Supercond.* (*SRF2005*), p. 314. Ithaca, NY: Cornell Univ. Press (2005)
17. Pekeler M, et al. *Proc. 12th Workshop RF Supercond.* (*SRF2005*), p. 331. Ithaca, NY: Cornell Univ. Press (2005)
18. Devanz G. *Proc. 12th Workshop RF Supercond.* (*SRF2005*), p. 108. Ithaca, NY: Cornell Univ. Press (2005)
19. Delayen JR. *Proc. 11th Workshop RF Supercond.* (*SRF2003*), pap. TuT01. Lübeck/Travemünde, Ger.: DESY (2003)
20. Facco A. *Proc. 12th Workshop RF Supercond.* (*SRF2005*), p. 21. Ithaca, NY: Cornell Univ. Press (2005)
21. Facco A. *Proc. 9th Eur. Part. Accel. Conf.* (*EPAC2004*), p. 142. Lucerne, Switz.: Eur. Phys. Soc. Accel. (2004)
22. Delayen JR. *Physica C* 441:1 (2006)
23. Simrock S. *Proc. 10th Workshop RF Supercond.* (*SRF2001*), p. 231. Tsukuba, Jpn.: KEK (2001)
24. Singer W, Brinkmann A, Proch D, Singer X. *Physica C* 386:379 (2003)
25. Mahner E, et al. *Proc. 6th Workshop RF Supercond.* (*SRF1993*), p. 1085. Newport News, VA: Jefferson Natl. Accel. Facil. (1993)
26. Kneisel P, et al. *Proc. 8th Workshop RF Supercond.* (*SRF1997*), p. 463. Abano Terme, Italy: INFN (1997)
27. Saito K, et al. *Proc. 4th Workshop RF Supercond.* (*SRF1989*), p. 635. Tsukuba, Jpn.: KEK (1989)
28. Higuchi T, et al. *Proc. 7th Int. Workshop RF Supercond.* (*SRF1995*), p. 723. Gif-sur-Yvette, Fr.: CEA-Saclay (1995)
29. Morgan A, et al. *Proc. 2007 Part. Accel. Conf.* (*PAC2007*), p. 2346. Piscataway, NJ: IEEE (2007)
30. Van der Horst B. *Proc. 13th Workshop RF Supercond.* (*SRF2007*), pap. TUP30. Beijing: Peking Univ. Press (2007)
31. Geng RL, et al. *Proc. 12th Workshop RF Supercond.* (*SRF2005*), p. 459. Ithaca, NY: Cornell Univ. Press (2005)
32. Furuta F, et al. *Proc. 3rd Int. Part. Accel. Conf.* (*IPAC2012*), p. 1918. Piscataway, NJ: IEEE (2012)
33. Cooper C, et al. *Proc. 15th Workshop RF Supercond.* (*SRF2011*), p. 571. JACoW.org: Jt. Accel. Conf. Website (2011)
34. Conway ZA, et al. *Proc. 14th Int. Workshop RF Supercond.* (*SRF2009*), p. 176. Berlin: Helmholtz (2009)
35. Saito K, et al. *Proc. 6th Workshop RF Supercond.* (*SRF1993*), p. 1151. Newport News, VA: Jefferson Natl. Accel. Facil. (1993)
36. Kneisel P, et al. *Proc. 6th Workshop RF Supercond.* (*SRF1993*), p. 628. Newport News, VA: Jefferson Natl. Accel. Facil. (1993)
37. Visentin B. *Proc. 6th Eur. Part. Accel. Conf.* (*EPAC1998*), 3:1885. London: Inst. Phys. (1998)
38. Lilje L, et al. *Proc. 9th Workshop RF Supercond.* (*SRF1999*), pap. TuA001. Santa Fe, NM: Los Alamos Natl. Lab. (1999)
39. Reschke D. *Proc. 12th Workshop RF Supercond.* (*SRF2005*), p. 71. Ithaca, NY: Cornell Univ. Press (2005)
40. Calatroni S. *Proc. 12th Workshop RF Supercond.* (*SRF2005*), p. 149. Ithaca, NY: Cornell Univ. Press (2005)
41. Therasse M, et al. *Proc. 2nd Int. Part. Accel. Conf.* (*IPAC2011*), p. 316. Piscataway, NJ: IEEE (2011)
42. Valente-Feliciano A-M. *Proc. 15th Workshop RF Supercond.* (*SRF2011*), p. 332. JACoW.org: Jt. Accel. Conf. Website (2011)
43. Krishnan M, et al. *Phys. Rev. Spec. Top. Accel. Beams* 15:032001 (2012)
44. Singer W. *Proc. 13th Workshop RF Supercond.* (*SRF2007*), pap.WE301. Beijing: Peking Univ. Press (2007)
45. Singer W. *Physica C* 441:89 (2006)
46. Palmieri V. *Proc. 11th Workshop RF Supercond.* (*SRF2003*), p. 357. Lübeck/Travemünde, Ger.: DESY (2003)

47. Singer W. *Proc. 12th Workshop RF Supercond.* (*SRF2005*), p. 143. Ithaca, NY: Cornell Univ. Press (2005)
48. Palmieri V. *Proc. 11th Workshop RF Supercond.* (*SRF2003*), pap. TuP26. Lübeck/Travemünde, Ger.: DESY (2003)
49. Myneni GR. *Proc. 12th Workshop RF Supercond.* (*SRF2005*), pap. MoP08. Ithaca, NY: Cornell Univ. Press (2005)
50. Kneisel P, et al. *Proc. 12th Workshop RF Supercond.* (*SRF2005*), p. 134. Ithaca, NY: Cornell Univ. Press (2005)
51. Singer W, et al. *Proc. 1st Int. Symp. Supercond. Sci. Technol. Ingot Niobium*, p. 13. Newport News, VA: Jefferson Natl. Accel. Facil. (2010)
52. Reschke D, et al. *Proc. 15th Workshop RF Supercond.* (*SRF2011*), p. 490. JACoW.org: Jt. Accel. Conf. Website (2011)
53. Geng R, et al. *Proc. 15th Workshop RF Supercond.* (*SRF2011*), p. 501. JACoW.org: Jt. Accel. Conf. Website (2011)
54. Aull S, et al. *Proc. 15th Workshop RF Supercond.* (*SRF2011*), p. 702: JACoW.org: Jt. Accel. Conf. Website (2011)
55. Geng RL, et al. *Proc. Part. Accel. Conf.* (*PAC2007*), p. 2337. Piscataway, NJ: IEEE (2007)
56. Vallet C, et al. *Proc. 3rd Eur. Part. Accel. Conf.* (*EPAC1992*), p. 1295. Berlin: Helmholtz (1992)
57. Romanenko A, Grassellino A, Melnychuk O, Sergatskov S. *J. Appl. Phys.* 115:184093 (2014)
58. Knobloch J. *Advanced thermometry studies of superconducting radio-frequency cavities*. PhD thesis. Dep. Phys., Cornell Univ. 350 pp. (1997)
59. Bonin B, Roth R. *Proc. 5th Workshop RF Supercond.* (*SRF1991*), p. 210. Hamburg: DESY (1991)
60. Smith JF. *Bull. Alloy Phase Diagr.* 4:39 (1983)
61. Barkov F, et al. *Phys. Rev. Spec. Top. Accel. Beams* 15:122001 (2012)
62. Barkov F, et al. *J. Appl. Phys.* 114:164904 (2013)
63. Norskov JK, Besenbacher F. *J. Less Common Metals* 130:475 (1987)
64. Romanenko A, et al. *Appl. Phys. Lett.* 102:232601 (2013)
65. Knobloch J, Padamsee H. *Proc. 8th Workshop RF Supercond.* (*SRF1997*), p. 345. Abano Terme, Italy: INFN (1997)
66. Dacca A, et al. *Appl. Surf. Sci.* 126:219 (1998)
67. Kowalski K. *Proc. 11th Workshop RF Supercond.* (*SRF2003*), p. 610. Lübeck/Travemünde, Ger.: DESY (2003)
68. Romanenko A, et al. *Phys. Rev. Spec. Top. Accel. Beams* 16:012001 (2013)
69. Valles NRA, et al. *Proc. 16th Int. Conf. RF Supercond.*, p. 300. JACoW.org: Jt. Accel. Conf. Website (2013)
70. Visentin B. *Proc. Workshop Push. Limits RF Supercond.*, p. 94. Argonne, IL: Argonne Natl. Lab. (2004)
71. Halbritter J. *Proc. 38th Eloisitron Workshop*, p. 59. Erice, Italy: World Sci. (2001)
72. Vines J, Xie Y, Padamsee H. *Proc. 13th Workshop RF Supercond.* (*SRF2007*), p. 178. Beijing: Peking Univ. Press (2007)
73. Bauer P. *Proc. 12th Workshop RF Supercond.* (*SRF2005*), p. 223. Ithaca, NY: Cornell Univ. Press (2005)
74. Gurevich A. *Physica C* 441:38 (2006)
75. Bauer P. *Proc. 12th Workshop RF Supercond.* (*SRF2005*), p. 223. Ithaca, NY: Cornell Univ. Press (2005)
76. Xie Y. *SRF Note 080108-05*. Ithaca, NY: Cornell Univ. (2008)
77. Graber J. *High power RF processing studies of 3 GHz niobium superconducting accelerator cavities.* PhD thesis. Dep. Phys., Cornell Univ. 236 pp. (1993)
78. Gonnella D, Liepe M. *Proc. 16th Int. Conf. RF Supercond.*, p. 475. JACoW.org: Jt. Accel. Conf. Website (2013)
79. Grassellino A, et al. *Supercond. Sci. Technol.* 26:102001 (2013)
80. Xiao BP, et al. *Physica C* 490:26 (2013)
81. Ciovati G. *Physica C* 441:44 (2006)
82. Visentin B. *Proc. 11th Workshop RF Supercond.* (*SRF2003*), p. 199. Lübeck/Travemünde, Ger.: DESY (2003)
83. Ciovati G. *Proc. 13th Workshop RF Supercond.* (*SRF2007*), p. 70. Beijing: Peking Univ. Press (2007)
84. Ciovati G, et al. *Phys. Rev. Spec. Top. Accel. Beams* 13:022002 (2010)

85. Romanenko A, Goncharova LV. *Supercond. Sci. Technol.* 24:105017 (2011)
86. Antoine CZ, et al. *Proc. 5th Workshop RF Supercond.* (*SRF1991*), p. 616. Hamburg: DESY (1991)
87. Tajima T, et al. *Proc. 11th Workshop RF Supercond.* (*SRF2003*), pap. THP19. Lübeck/Travemünde, Ger.: DESY (2003)
88. Romanenko A, et al. *Supercond. Sci. Technol.* 26:035003 (2013)
89. Romanenko A, et al. *Appl. Phys. Lett.* 102:232601 (2013)
90. Klein U, Proch D. *Proc. Conf. Future Possibilities Electron Accel.*, p. N1. Charlottesville: Univ. Va. Press (1979); Klein U, Proch D. *Wuppertal Rep.* WUB78–31 (1979)
91. Padamsee H, et al. *IEEE Trans. Magn.* 19:1322 (1983)
92. Niedermann P. *Experiments on enhanced field emission*. PhD thesis no. 2197, Univ. Geneva. 150 pp. (1986)
93. Mahner E. *Proc. 6th Workshop RF Supercond.* (*SRF1993*), p. 252. Newport News, VA: Jefferson Natl. Accel. Facil. (1993)
94. Crawford C, et al. *Part. Accel.* 49:1 (1995)
95. Reschke D. *Proc. Workshop Push. Limits RF Supercond.*, p. 167. Argonne, IL: Argonne Natl. Lab. (2004)
96. Conway ZA, et al. *Proc. 14th Int. Workshop RF Supercond.* (*SRF2009*), p. 113. Berlin: Helmholtz (2009)
97. Singer W. *Proc. 13th Workshop RF Supercond.* (*SRF2007*), pap. TuT3a. Beijing: Peking Univ. Press (2007)
98. Piel H. *Proc. CERN Accel. Sch.*, p. 149. Hamburg: DESY (1989)
99. Geng RL. *Limits in cavity performance*. Presented at Workshop on RF Superconductivity (SRF2011), 15th, Argonne, IL. **https://twindico.hep.anl.gov/indico/conferenceOtherViews.py?view=standard&confId=631** (2011)
100. Iwashita Y, Tajima Y, Hayano H. *Phys. Rev. Spec. Top. Accel. Beams* 11:093501 (2008)
101. Cooley LD, et al. *IEEE Trans. Appl. Supercond.* 21:2609 (2011)
102. Geng RL, et al. *Proc. 13th Workshop RF Supercond.* (*SRF2007*), p. 575. Beijing: Peking Univ. Press (2007)
103. Watanabe K, et al. *Proc. 1st Int. Part. Accel. Conf.* (*IPAC2010*), p. 2965. Piscataway, NJ: IEEE (2010)
104. Padamsee H. *IEEE Trans. Magn.* 21:149 (1985)
105. Kako E, et al. *Proc. 9th Workshop RF Supercond.* (*SRF1999*), p. 179. Santa Fe, NM: Los Alamos Natl. Lab. (1999)
106. Kneisel P, et al. *Proc. 2005 Part. Accel. Conf.* (*PAC2005*), p. 3955. Piscataway, NJ: IEEE (2005)
107. Matricon J, Saint-James D. *Phys. Lett. A* 24:241 (1967)
108. Transtrum MK, Catelani G, Sethna JP. *Phys. Rev. B* 83:094505 (2011)
109. Catelani G, Sethna JP. *Phys. Rev. B* 78:224509 (2008)
110. Hays T, Padamsee H. *Proc. Part. Accel. Conf.* (*PAC1995*), p. 1617. Piscataway, NJ: IEEE (1996)
111. Campisi IE. *IEEE Trans. Magn.* 25:134 (1985)
112. Valles N, Liepe M. *Proc. 15th Workshop RF Supercond.* (*SRF2011*), pap. TuP064. JACoW.org: Jt. Accel. Conf. Website (2011)
113. Gurevich A. *Appl. Phys. Lett.* 88:012511 (2006)
114. Posen S, et al. *Proc. 16th Int. Conf. RF Supercond.* (*SRF2013*), p. 794. JACoW.org: Jt. Accel. Conf. Website (2013)
115. Butterworth A, et al. *Nucl. Instrum. Methods A* 587:151 (2008)
116. Leeman C, Douglas D, Krafft G. *Annu. Rev. Nucl. Part. Sci.* 51:413 (2001)
117. Maesen P, Ciapala E, Pechaud G. *Proc. 13th Workshop RF Supercond.* (*SRF2007*), p. 512. Beijing: Peking Univ. Press (2007)
118. Hogan J, et al. *Proc. 3rd Int. Part. Accel. Conf.* (*IPAC2012*), p. 2429. Piscataway, NJ: IEEE (2012)
119. Benson SV, et al. *J. Phys. Conf. Ser.* 299:012014 (2011)
120. Padamsee H. *Proc. 5th Workshop RF Supercond.* (*SRF1991*), p. 963. Hamburg: DESY (1991)
121. Padamsee H. *Proc. 1st TESLA Workshop*, CLNS90-1029. Ithaca, NY: Cornell Univ. Press (1990)
122. Rossbach J. *Nucl. Instrum. Methods A* 375:269 (1996)
123. Vogt M, et al. *Proc. 4th Int. Part. Accel. Conf.* (*IPAC2013*), p. 1167. Piscataway, NJ: IEEE (2013)
124. Honkavaara K, et al. *Proc. 3rd Int. Part. Accel. Conf.* (*IPAC2012*), p. 1918. Piscataway, NJ: IEEE (2012)
125. Vogel E, et al. *Proc. 1st Int. Part. Accel. Conf. 2010* (*IPAC2010*), p. 4281. Piscataway, NJ: IEEE (2010)
126. DESY XFEL Proj. Group. *The Technical Design Report of the European XFEL.* DESY2006-097. **http://xfel.desy.de/localfsExplorer_read?currentPath=/afs/desy.de/group/xfel/wof/EPT/TDR/XFEL-TDR-final.pdf** (2007)

127. Yamamoto A, Ross MC, Walker NJ. *Proc. 15th Workshop RF Supercond.* (*SRF2011*), p. 7. JACoW.org: Jt. Accel. Conf. Website (2011)
128. Belomestnykh S. *Proc. 13th Workshop RF Supercond.*, pap. MO302. Beijing: Peking Univ. Press (2007)
129. Liepe M, et al. *Proc. 15th Workshop RF Supercond.*, p. 90. JACoW.org: Jt. Accel. Conf. Website (2011)
130. Nakamura N. *Proc. 3rd Int. Part. Accel. Conf.* (*IPAC2012*), p. 1040. Piscataway, NJ: IEEE (2012)
131. Holtkamp N. *Proc. 2003 Part. Accel. Conf.* (*PAC2003*), p. 11. Piscataway, NJ: IEEE (2003)
132. Kim S-H. *Proc. 14th Int. Workshop RF Supercond.* (*SRF2009*), p. 11. Berlin: Helmholtz (2008)
133. Danared H. In *Proc. 3rd Int. Part. Accel. Conf.* (*IPAC2012*), p. 3904. Piscataway, NJ: IEEE (2012)
134. Khabiboulline T, et al. *Proc. 3rd Int. Part. Accel. Conf.* (*IPAC2012*), p. 2330. Piscataway, NJ: IEEE (2012)
135. Fuerst JD, et al. *Proc. 14th Int. Workshop RF Supercond.* (*SRF2009*), p. 52. Berlin: Helmholtz (2009)
136. Kelly M, et al. *Proc. 26th Linear Accel. Conf.*, p. 348. JACoW.org: Jt. Accel. Conf. Website (2012)
137. Ferdinand R, et al. *Proc. 16th Int. Conf. RF Supercond.* (*SRF2013*), p. 11. JACoW.org: Jt. Accel. Conf. Website (2013)
138. Leitner M, et al. *Proc. 16th Int. Conf. RF Supercond.* (*SRF2013*), p. 1. JACoW.org: Jt. Accel. Conf. Website (2013)

Annual Review of Nuclear and Particle Science

Volume 64, 2014

Contents

Index

Errata

An online log of corrections to *Annual Review of Nuclear and Particle Science* articles may be found at http://www.annualreviews.org/errata/nucl